Chapter 2

An Ultrasound-Guided Mechatronics-Assisted System for Semi-Automated Seed Implantation and Tracking in Prostate Brachytherapy

Carlos Rossa,[1,*] *Jay Carriere*,[2] *Mohsen Khadem*,[3]
Ronald Sloboda,[4] *Nawaid Usmani*[4] and *Mahdi Tavakoli*[5]

1. Introduction

Prostate cancer is the most prevalent non-skin malignancy in men worldwide. Among the various treatment options that are available including surgery, external beam radiotherapy, and hormone therapy, transperineal interstitial permanent prostate brachytherapy (TIPPB) using radioactive seeds has emerged as an efficacious, minimally-invasive, patient-friendly, and cost-effective treatment option for localized prostate cancer. The robust clinical outcomes reported in the prostate brachytherapy literature highlight the great efficacy of this treatment modality when employed at cen-

[1] Department of Computer and Systems Engineering, Carleton University, Ottawa, ON, Canada.

[2] Department of Electrical and Computer Engineering, University of Calgary, Calgary, AB, Canada. Email: jay.carriere@ucalgary.ca

[3] School of Informatics, University of Edinburgh, Edinburgh, United Kingdom. Email: mohsen.khadem@ed.ac.uk

[4] Cross Cancer Institute and the Department of Oncology, University of Alberta, Canada. Emails: ron.sloboda; nawaid.usmani@albertahealthservices.ca

[5] Department of Electrical and Computer Engineering, University of Alberta, Edmonton, AB, Canada. Email: mahdi.tavakoli@ualberta.ca

* Corresponding author: rossa@sce.carleton.ca

tres performing high quality implants. However, brachytherapy is a technical procedure that relies on surgeons with sufficient expertise and case volume to maintain the quality of implants required to achieve these results.

Close scrutiny of TIPPB's technical aspects indicates room for considerable improvement. Contemporary brachytherapy techniques treat the whole prostate and involve the insertion of needles through the perineum using a template grid under ultrasound guidance. These seed-carrying needles are manually guided toward planned locations in the prostate, where the seeds are deposited, assuming that the needles will remain parallel across the entire length of their insertion. However, in practice, this assumption does not hold particularly well, causing the actual needle trajectories to not pass through the planned locations. Contributing to this error are prostate deformation/motion during needle insertion, imaging limitations, needle placement uncertainty Nath et al. (2000); Webster et al. (2006); Khadem et al. (2016), prostate swelling during implantation Sloboda et al. (2010), and seed migration Usmani et al. (2011). Experienced physicians can place seeds with an average absolute accuracy of no better than 5 mm, a substantial error of more than 10% of the average prostate diameter Taschereau et al. (2000).

Due to the currently limited accuracy of delivering seeds, brachytherapy has been limited to primarily treating the entire prostate gland for patients with localized prostate cancer. Treating the whole gland may result in side-effects such as urinary and rectal toxicity due to the effects on the adjacent structures. In the near future, anticipated focal treatment of dominant intraprostatic lesions identified by cancer-specific Magnetic Resonance Imaging (MRI) and Positron Emission Tomography (PET) imaging will require that seed placement accuracy must improve substantially. Improving source placement can result in enhanced treatment of localized prostate cancer by brachytherapy, and in addition will make this treatment modality applicable to other clinical situations. It has been estimated that between one-half to two-thirds of men with early stages of prostate cancer may be amenable to focal therapy Karavitakis et al. (2011); Bott et al. (2010).

To improve seed placement accuracy, robotics assisted needle steering and seed implantation have been proposed Podder et al. (2014); Muntener et al. (2006); Patriciu et al. (2007); Cowan et al. (2011); Rossa et al. (2016); Phee et al. (2006); Salcudean et al. (2008); Wei et al. (2004). To steer the seed-carrying needles, these systems either rotate the needle base on a measured basis during

insertion, or apply forces at the base in order to control the needle tip's trajectory. The needle insertion can be performed manually Schneider et al. (2004) or automatically Muntener et al. (2006); Patriciu et al. (2007) while the robot orients the needle inside the tissue Schneider et al. (2004). In term of the degree of automation, these systems can essentially be classified into three main categories:

- *Fully automated steering*: The system automatically performs the needle insertion and the seed deposition in tissue Patriciu et al. (2007); Muntener et al. (2006); Phee et al. (2006); Meltsner et al. (2007); Adebar et al. (2011); Hungr et al. (2012); Yu et al. (2006); Phee et al. (2006). Although high accuracy can be achieved, integrating these systems with current clinical practice is challenging and most often, several modifications to the clinical setting are necessary.

- *Semi-automated steering*: The robotic system acts as a needle holder that either rotates the needle axially or manipulates the needle shaft Wei et al. (2004); Fichtinger et al. (2008); Schneider et al. (2004); Salcudean et al. (2008) with the physician being in charge of the insertion procedure. This category includes teleoperated needle insertion schemes Seifabadi et al. (2012).

- *Fully manual steering*: This class comprises technologies designed to provide the physician with relevant information about the necessary manoeuvres and keeps her/him in control of both insertion and steering procedures, such as visual and tactile feedback devices Rossa et al. (2016); Magee et al. (2007); Basu et al. (2016).

The first two categories often make use of complex structures that need to be integrated with the current clinical setting. In the third category, the implant outcomes still depend on the surgeon's ability to perform the necessary steering actions.

In Rossa et al. (2016), we introduced a new twist on robotic-assisted needle steering that uses a fully hand-held apparatus for accurate needle steering (see Fig. 1(a)). The device automatically rotates the needle at appropriate insertion depths as the surgeon manually inserts it. The system was designed to be entirely compatible with the current operating room setting, and hence, does not rely on any complex structures. In this paper, we extend this

new framework to accurate seed implantation and tracking using ultrasound images in focal low dose rate brachytherapy.

Contributions of this paper include: (i) The device is modified to incorporate a miniature force sensor that measures the tissue parameters required in the needle steering controller online. (ii) A new needle steering controller based on the Rapidly Exploring Random Tree algorithm is implemented, and (iii) a method is devised to track the position of each implanted seed on-line. The concept is validated by implanting dummy seeds in biological and synthetic tissue samples in order to achieve a hypothetical desired seed distribution. Experimental results obtained from 90 seed implants indicate an accuracy of 0.46 mm in delivering the seeds. This is the first implementation of a fully hand-held seed implantation and tracking system for the emerging modality of focal prostate cancer treatment.

2. The Hand-Held Apparatus for Seed Implant

In order to perform needle insertion and seed deposition, we modified the needle steering device previously presented in Rossa et al. (2016) (for a video please see `https://goo.gl/Z7jJp5`) (see Fig. 1(a)). Standard brachytherapy needles are connected to the apparatus, which can rotate the needle base axially (see Fig. 1(b)). As the surgeon uses the device to insert the needle, the 3D position of the apparatus is measured in real time by an optical motion tracker that follows markers placed on the side of the device (not visible in Fig. 1(a)). An important difference compared to the device presented in Rossa et al. (2016) is that in this paper, a compression/traction sensor (model LSB200 S-Beam from Futek, Irvine, USA) is embedded in the device in order to measure the axial force applied to the needle base during insertion and withdrawal. The goal is to employ the force measurements from the two 1-DOF force sensors during needle insertion and withdrawal to estimate the forces applied by the tissue onto the needle tip, such that future needle deflection can be predicted by a mechanics-based model and the necessary corrective action taken by the hand-held apparatus.
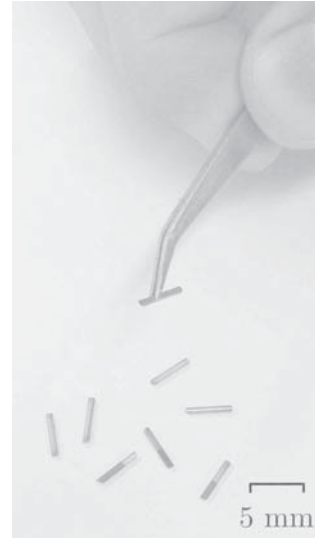
To simulate radioactive brachytherapy seeds, the dummy seeds made of 5 mm long, 1 mm in diameter, stainless steel cylinders, shown in Fig. 1(c), were fabricated. A single seed and a stylet are loaded in the needle. Once the needle reaches the desired depth, the
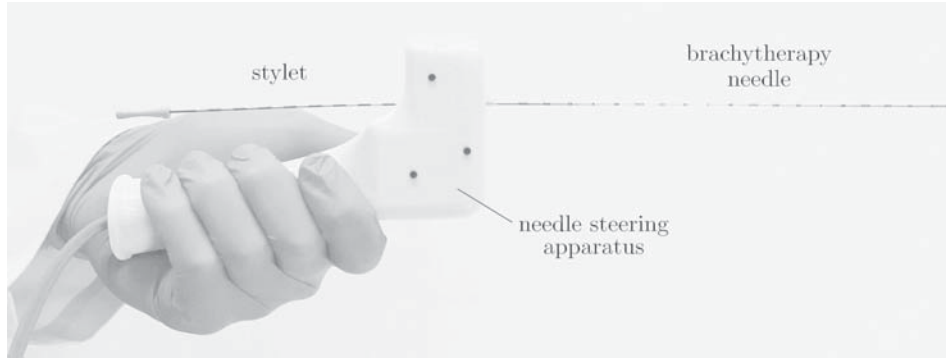
(a) The neele steering device
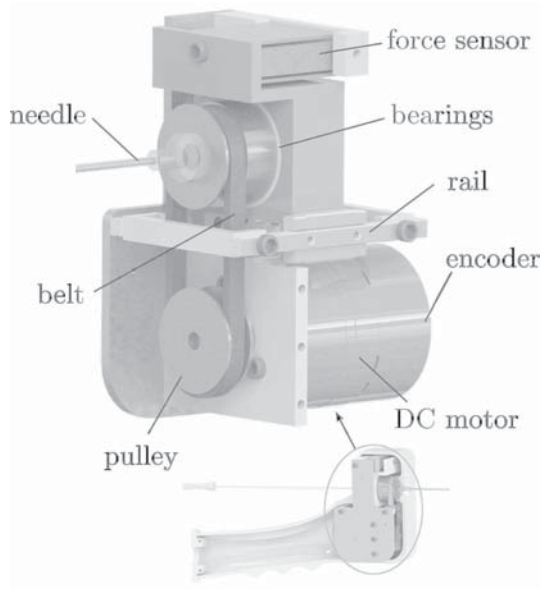
(b) Actuation unit

(c) Dummy seeds

Figure 1: In (a), the needle steering device introduced in Rossa et al. (2016) is shown. (b) presents the upgraded actuation unit that comprises a 1-DOF force sensor that measures the needle insertion and withdrawal forces. The device steers the needle and is used to deposit the dummy seeds shown in (c).

surgeon holds the stylet in place and withdraws the needle (with the device) such that the stylet removes the seed from the needle shaft for deposition in tissue.

3. Needle Steering Controller

This section presents the model and steering algorithm that are combined to steer the needle towards the target.

3.1 Needle-Tissue Modelling

We will employ the needle-tissue interaction model we presented in Rossa et al. (2016). The inputs to the model are the needle insertion depth, the current needle deflection, and the rotation depth(s). The model outputs the future needle tip trajectory and the needle shape. In Rossa et al. (2016), the needle is modelled as a cantilever compliant beam that experiences forces applied by the tissue in the form of 1) a needle-tissue cutting force, which is applied at the needle tip normal to the needle shaft (denoted by F), and 2) the tissue reaction force applied along the needle shaft, which is due to compression of the tissue. This latter force depends on the stiffness of tissue per unit length of the needle (denoted by K).

In Rossa et al. (2016), a method is devised to estimate both F and K based only on ultrasound images. However, this requires the ultrasound probe to follow the needle during insertion. Thanks to the force sensor added to the actuation unit, F can be measured without need for image feedback. Once F is determined, K can be found by fitting the model to a single deflection measurement point obtained from a stationary ultrasound probe.

In order to calculate the force F applied at the needle tip, the needle steering apparatus measures the forces applied to the needle's base F_{in} that are necessary to insert and withdraw it from the tissue (see 2(a)). From this information, we will derive F by following the procedure shown in Fig. 2. In Fig. 2(a), as the needle is pushed into tissue, a force F_c is applied at the needle tip, that has transverse and longitudinal components Q, and F, respectively. These forces are functions of F_c and of the needle bevel angle β. As the surgeon pushes the needle into the tissue, the measured force at the needle base F_{in} corresponds to $F_1 = P + f$ where f is the needle-tissue frictional force along the shaft given by $f = (bv_1)d$, where v_1 is the insertion velocity, and b is the friction coefficient per unit length of the inserted needle. When the needle is withdrawn after insertion, the measured force F_2 corresponds to friction only. If the needle is withdrawn with a velocity of v_2, the force P can be found as

$$P = F_1 - F_2 \left(\frac{v_1}{v_2} \right) \tag{1}$$

It is thereby implied that b is constant during insertion and withdrawal Khadem et al. (2016). The force F is finally computed as $F = P(\tan \beta)^{-1}$, where β is the needle bevel angle. Knowing F, one can determine K by fitting the model such that the estimated

(a) Insertion: $F_1 = F_r + P$

(b) Withdrawal $F_2 = F_r$
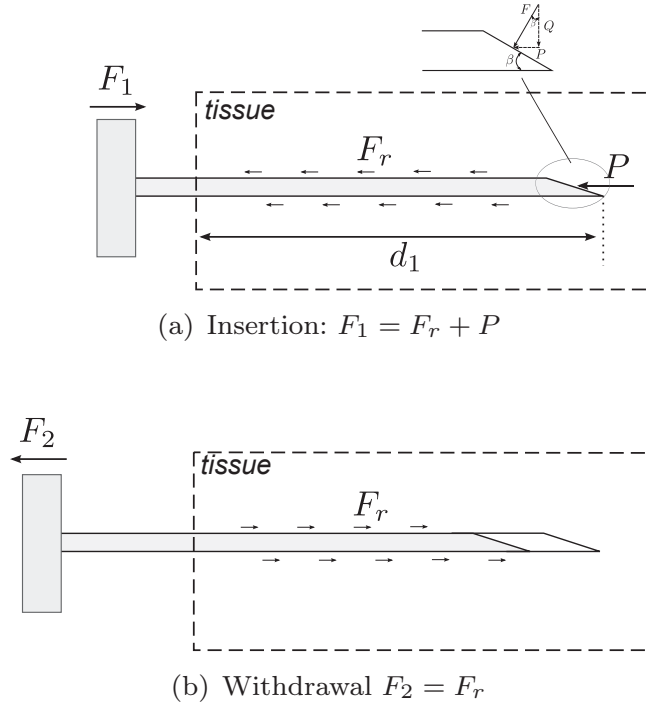
Figure 2: Needle insertion in soft tissue. As the needle cuts a path in the tissue, a force F_c is applied to the needle tip. The horizontal component of F_c plus friction along the shaft correspond to the needle insertion force measured at the needle base. During needle withdrawal, the measured force corresponds to friction only.

needle deflection $\hat{v}_i(K)$ matches the measured deflection v_i of an inserted needle, at a point i along its shaft. More specifically, K is found to minimize

$$J(K) = \min \sum_{i=1}^{n} (v_i - \hat{v}_i(K))^2, \tag{2}$$

where n is the number of measurements taken.

Once the needle-tissue model parameters are identified, the model can be used to estimate the optimal needle rotation depths as described in the next subsection.

3.2 *Needle Steering Controller*

In this section, a novel motion planner is developed. The motion planner computes a large number of needle tip trajectories (plans) using the model presented in Rossa et al. (2016) and selects the best plan. It outputs a set of depths at which the needle is axially rotated that brings the needle to the target. The planner

uses the Rapidly Exploring Random Tree (RRT) algorithm LaValle and Kuffner (2001); Patil et al. (2014) to calculate the rotation depths. RRT is an efficient sampling algorithm to quickly search high-dimensional spaces that have algebraic constraints such as the number of allowed needle rotations, by randomly building a space-filling tree. Figure 3(a) shows a block diagram of the closed-loop control algorithm based on the online motion planning.

To design the online motion planner we present the needle steering problem in the needle configuration space, called $\mathcal{C}$. Assuming the needle moves in a 2D insertion plane, the needle workspace is a Euclidean space $\mathcal{W} = \mathbb{R}^2$. The configuration space ($\mathcal{C}$) is the space of all possible control actions (i.e., depth(s) of needle rotation(s)), whose values identify the configuration of the needle tip in the workspace. Considering symmetry of rotation depths (e.g., rotations at depths of 40 and 80 mm are equal to rotations at 80 and 40 mm) the configuration space is an n-dimensional simplex, where n is the number of axial rotations. For instance, if the maximum allowable number of rotations is 3, the configuration space forms a tetrahedron.

The proposed motion planner uses an approximate decomposition of $\mathcal{C}$. Assuming that the distance between two consecutive rotations is at least 5 mm, $\mathcal{C}$ can be decomposed into several smaller simplices shown in Fig. 3(c). This is a valid assumption since two close 180° axial rotations are equal to one 360° rotation of the needle tip and this action has no effect on needle deflection.

The disjoint cells in $\mathcal{C}$ form a *connectivity graph*. The nodes of this graph are vertices of the cells corresponding to a certain configuration (i.e., rotation depths). Assuming that the initial guess for a configuration in $\mathcal{C}$ is q_s and the goal configuration that steers the needle toward the target is q_g, planning a motion for the needle involves searching the connectivity graph for a path from cell containing q_s to the cell containing q_g. For this purpose we use the RRT algorithm. In the following a pseudocode description of the motion planner algorithm is given.

The inputs of the RRT are the current depth X_0, the number of allowed rotations N, and the computation time available for planning T_{max}. A hypothetical example of tree generation for $N = 2$ is shown in Fig. 3(b). First, the configuration space $\mathcal{C}$ is formed based on the number of allowed rotations N and the current needle insertion depth $X_0 = 0$. The tree is initialized with a first vertex q_s located at $(0, 0)$ (see (I) in Fig. 3(b)). The algorithm then generates a random candidate q_{rand} from the N-dimentional
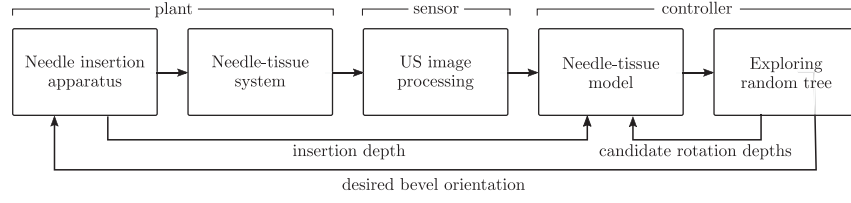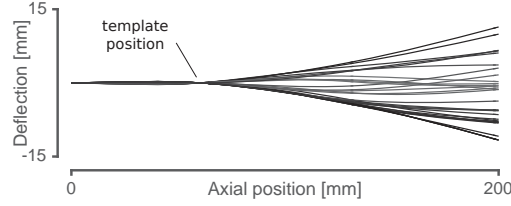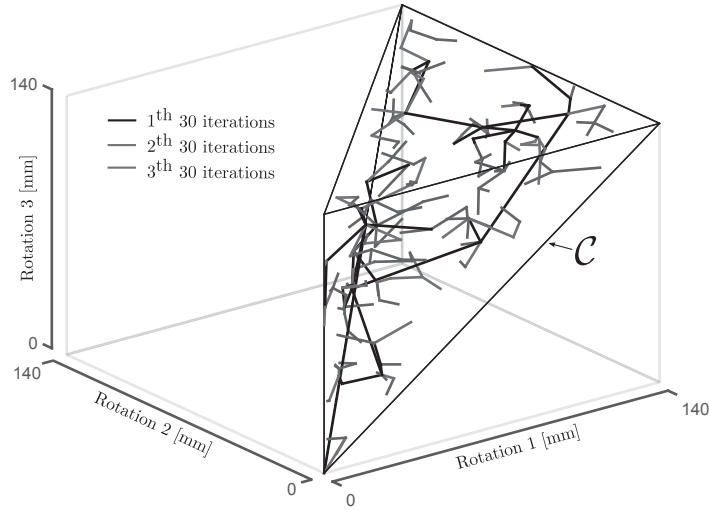
(a) Diagram of the needle steering system
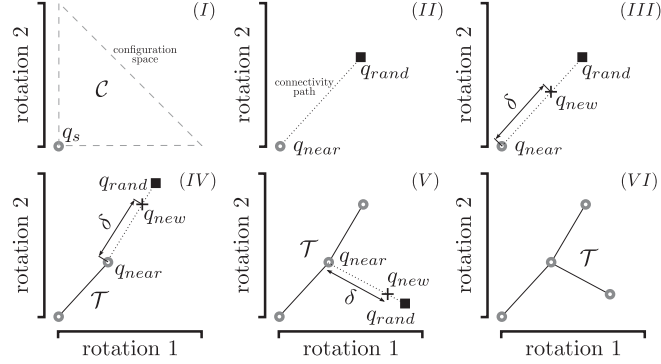
(b) Hypothetical 2D tree generation

(c) Work space: Needle shaft deflection

(d) 3D tree in the configuratin space

Figure 3: Overview of needle steering controller. (a) shows the block diagram of the needle steering system. In (b), the RRT algorithm evaluates the needle targeting accuracy for different rotation depths as shown in (c). In (d) the resultant set of rotation depths.

configuration space $\mathcal{C}$ (See `Rand_Conf` in Algorithm 1 and (II) in Fig. 3(b)). Next, `Near_Vertex` runs through all the vertices (candidate rotation depths) in $\mathcal{C}$ to find the closest vertex to q_{rand}. `New_Conf` produces a new candidate configuration q_{new} on the segment joining q_{near} to q_{rand} at a predefined arbitrary distance δ from q_{near} (see (III) in Fig. 3(b)).

Algorithm 1: $q_{goal} \longleftarrow$ `RRT_Algorithm` (X_0, N, T_{max})

$\mathcal{C} \longleftarrow$ `Initialize_space` (X_0, N)
$\mathcal{T} \longleftarrow$ `Initialize_tree` $(X_\bullet, N)$
while $\chi = \varnothing \wedge \Gamma < \Gamma_{max}$ **do**
    $q_{rand} \longleftarrow$ `Rand_Conf` $(\mathcal{C})$
    $q_{near} \longleftarrow$ `Near_Vertex` $(q_{rand}, \mathcal{C})$
    $q_{new} \longleftarrow$ `New_Conf` (q_{rand}, q_{near})
    $p_{new} \longleftarrow$ `Needle-tissue-model` *Rossa et al. (2016)*
      (q_{new})
    $\mathcal{T} \longleftarrow$ `Add_Vertex`(q_{new})
    $\mathcal{T} \longleftarrow$ `Add_Edge`(q_{new}, q_{near})
    if $p_{new} \in \mathcal{G}$ **then**
      $\mid$ $q_{goal} \longleftarrow$ `Extract_Conf`(q_{new})
    end
end

The random tree $\mathcal{T}$ is expanded by incorporating q_{new} and the segment joining it to q_{near}, as shown in (VI). Next, the needle tip path and targeting accuracy (p_{new}) are obtained by inputting the selected rotation depths in the needle-tissue interaction model Rossa et al. (2016). The predicted needle shape for various candidate sets of rotation depths is shown in Fig. 3(c). When the needle path for the newly added configuration is found to lie in the target region ($\mathcal{G}$), or when the computation times exceeds T_{max} the RRT planner terminates. The target region is a closed circle with 1 mm diameter, centred on the desired target location in $\mathcal{W}$. The former condition implies that when the estimated needle tip deflection at the maximum depth is less than 0.5 mm, the algorithm stops. If the stopping condition is not met, the algorithm continues to expand the tree with new vertices as depicted in (V) and (VI) in Fig. 3(b).

Once the algorithm stops, the output q_{goal} contains the best set of rotation depths that will bring the needle towards $\mathcal{G}$. The RRT expansion procedure results in a very efficient exploration of $\mathcal{C}$ and the procedure for generating new candidates in RRT is intrinsically biased toward regions of $\mathcal{C}$ that have not been visited.

In prostate brachytherapy, the needle insertion point and the target are typically on the same horizontal line. Throughout this

paper, we assume that the target is at a depth of 140 mm. In order to limit tissue trauma, the total number of needle axial rotations is set to three. Results of the simulation of the motion planner in configuration space $\mathcal{C}$ and the corresponding needle deflection predictions in needle workspace $\mathcal{W}$ for an insertion depth of 140 mm starting at 0 mm are shown in Fig. 3(c) and Fig. 3(d), respectively.

The RRT has been used for needle steering in LaValle and Kuffner (2001). Unlike LaValle and Kuffner (2001), our search space is directly constrained by the possible control inputs and by the number and depths of rotations. Therefore, there is no need to solve for the inverse kinematics of the model, which enables the optimization problem to be solved faster and makes the solution method suitable for online applications.

4. Experimental Setup

The setup for semi-automated seed implant is presented in Fig. 4. Please see the attached video. Standard 18-gauge clinical brachytherapy needles (Eckert & Ziegler Inc., USA) are loaded with a single dummy seed shown in Fig. 8(a) and connected to the needle steering apparatus. As in manual brachytherapy, a stylet is inserted in the needle shaft in order to deposit the seed in the tissue.
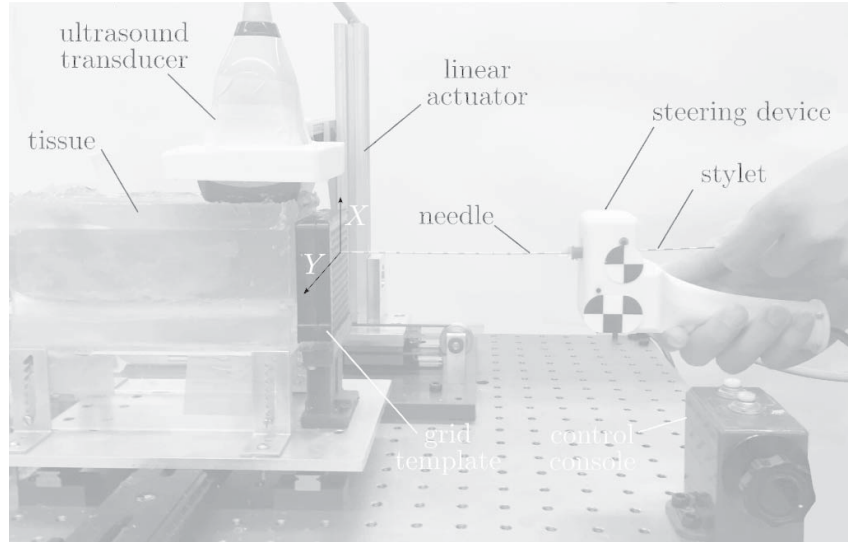
Figure 4: Experimental setup. A standard 18-gauge brachytherapy needle carrying a single dummy seed is inserted in the tissue through a guiding template. An ultrasound probe monitors the position of the needle tip.
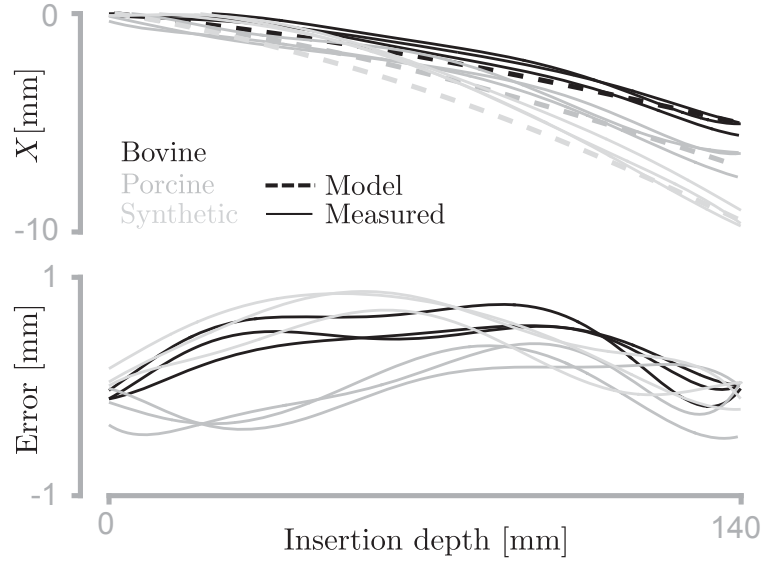
Figure 5: Model fit results for each tissue sample. The model parameters are found by minimizing the difference between the measured and estimated needle tip deflection at the depth of 140 mm.

The needle is inserted through a standard brachytherapy template grid (D0240018BK, from CR Bard, USA). For further details on the hardware implementation, we refer the reader to Rossa et al. (2016).

A 4DL14-5/38 linear ultrasound probe is placed on the tissue surface to acquire transverse 2D ultrasound images of the needle at 30 Hz. A linear stage motorized by a DC motor controls the position of the ultrasound probe using a discrete PID controller.

Three different tissues are used in the experiments. The first tissue is made by encasing a 130 mm long piece of porcine tissue into a mixture of 20% gelatin derived from acid-cured tissue (gel strength 300 from Sigma-Aldrich Corporation, USA) per litre of water. This tissue can be seen in Fig. 4. The gelatin is meant to create a 20 mm layer of tissue through which the needle is inserted before reaching the porcine tissue, and also to create a flat surface in order to ensure good acoustic contact between the ultrasound probe and the tissue. In the second tissue, the porcine layer is replaced with bovine tissue. Hence, the first two tissues are composed of two different layers. The third tissue is made of high friction plastisol gel (M-F Manufacturing Co., USA) mixed with 20% plastic softener.

For each tissue, 15 needle insertions at different locations in the grid template followed by deposition of a single seed are performed. The seeds are deposited at a depth of 140 mm. For each tissue, a set of 15 insertions is performed using an open loop controller (image

feedback is not used), and another set of 15 implants is performed using a closed-loop needle insertion controller. This amounts to a total of 6 different experimental scenarios and 90 seed implants in total.

Each seed implantation procedure is composed of three phases:

1. *Phase 1–Pre-scan*: The needle has not been inserted in the tissue. The ultrasound moves with a constant velocity of 8 mm·s^{-1} up to a depth of 150 mm and returns to the initial position. Thereby, all previously implanted seeds and tracks in the tissue left by other insertions can be identified.

2. *Phase 2–Needle insertion*: The ultrasound imaging plane is placed close to the needle tip. During insertion, the ultrasound probe moves in synchrony such that the needle tip is
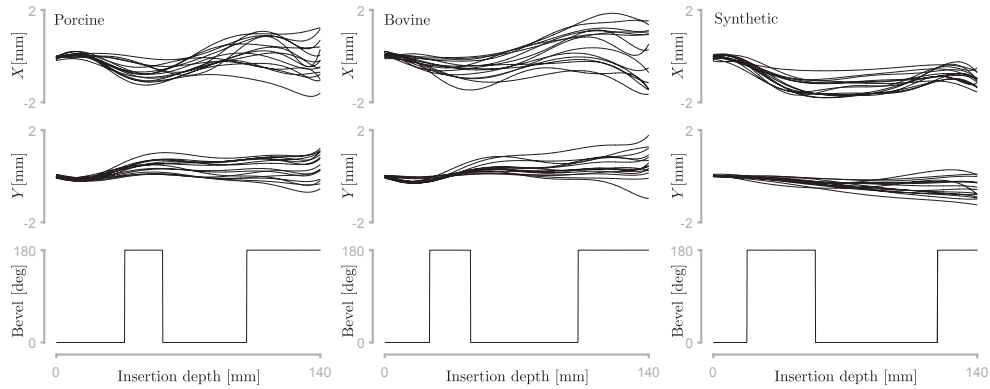
(a) Open loop needle steering results
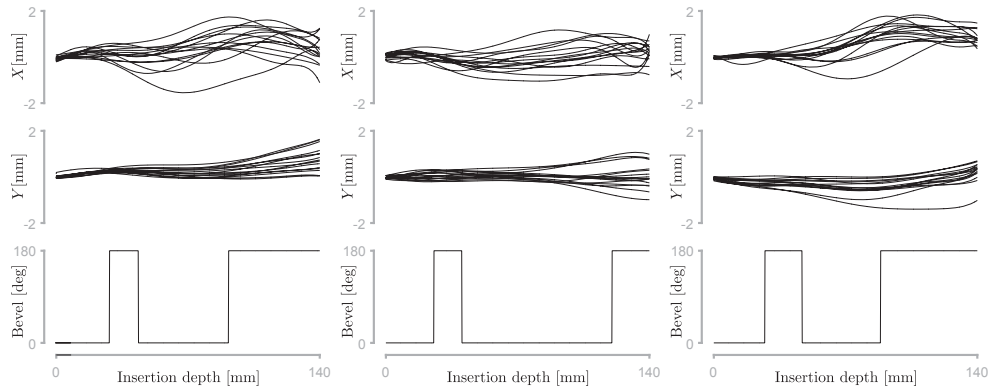
(b) Closed loop needle steering results

Figure 6: Path followed by the needle tip in the X and Y planes (defined in Fig. 4) during insertion in porcine, bovine, and synthetic tissue and the average position of the bevel angle using open loop (a) and closed loop (b) controllers, for each of the 15 insertions. Only the deflection in the X plane is controlled.

always visible in the image. Once the needle reaches the desired depth of 140 mm, the seed is manually deposited and the needle is withdrawn.

3. *Phase 3–Post-scan*: After the needle is withdrawn the tissue is scanned in order to identify the position of the seed deposited in Phase 2.

The needle steering controller will be employed in two different ways. In *open-loop* mode, the controller determines 3 optimal rotation depths prior to needle insertion. In *closed-loop* mode, the RRT controller updates the rotation online based on the measured needle tip position. The maximum computation time allowed for planning is 1 second, which was found to provide good convergence. The needle bevel angle is initially oriented such that the needle deflects in a plane that is parallel to the table shown in Fig. 4. Deflection along the vertical plane is not controlled.

4.1 Needle and Seed Tracking in Ultrasound Images

Needle tip tracking is done online as the needle is inserted into the tissue. Each transverse ultrasound image is processed in real-time using the algorithm presented in Waine et al. (2016). Seed localization is done using the information from both the Phase 3 scan, containing the implanted seed, and the Phase 1 scan, which is used to reduce background noise in the Phase 3 transverse images. Final implanted seed positions are obtained offline after Phase 3 scan is completed. Note that when *open-loop* needle steering is used, the images are not used as feedback in the controller but the needle tip is still tracked.

From the final needle tip position in Phase 2, the seed deposition depth is obtained and the transverse ultrasound image that contains the seed can be selected from the Phase 3 scan, which we will denote as I_{P3}. The original image obtained in Phase 3 is shown in Fig. 7(b). Even with the deposition depth of the seed known, seed localization in transverse images is complicated by several factors, the most important of which is that previous seeds are present alongside the target seed, as well as the seed not being very distinct from the background image noise. An additional complication is that the implanted seed moves away from the final needle tip location, found in Phase 2, as the needle is withdrawn.

The seed tracking algorithm consists of 2 stages, i.e., a pre-processing stage and the background noise removal, see Fig. 7(a). The first step in the pre-processing stage is to define a region of interest (ROI) around the final needle tip location, found in Phase 2, in I_{P3} that is large enough to capture the seed with moderate motion. Empirically, an ROI of 100 px by 100 px is found to be sufficient. The next step is to find the ultrasound image at the seed deposition depth captured in Phase 1, which we will call I_{P1}. This image contains the previously deposited seeds as well as background noise from the phantom tissue. In order to remove the noise and other seeds from the ROI in I_{P3} the exact same ROI is taken from I_{P1} and the background is removed through a subtraction, such that a cleaner image, denoted I_C, is created, where $I_C = |I_{P3} - I_{P1}|$. The image I_C is then enhanced through the same contrast stretching method given in Waine et al. (2016), see Fig. 7(b).

With the background noise and previous seeds removed from the image, the target seed is now quite distinct from the background and so the final step is the seed segmentation. A straightforward binary threshold, determined empirically to count any pixel with an intensity above 150 (on a scale from 0 to 255). As a final segmentation step all 4-connected component objects in the binary image are found and the object with the largest number of pixels is chosen as the seed. The seed location is then determined by taking the x and y centroids of all of the pixels in the seed's 4-connected object. Please see the attached video or visit `https://youtu.be/tnWdMXSxmiU`.

5. Experimental Results

This section is divided into three main parts. First, calibration of the needle steering controller is presented. Next, the needle steering and seed implant results are shown.

5.1 Model Identification

The first step in performing assisted needle steering for accurate seed deposition is to calibrate the needle steering controller. To this end, 3 needle insertions followed by withdrawals are performed in each tissue at an average velocity of 2 mm·s^{-1}. The controller is turned off and the needle insertion/withdrawal force is recorded. For verification purposes, the ultrasound probe is following the needle tip. However, in a clinical scenario the ultrasound probe could
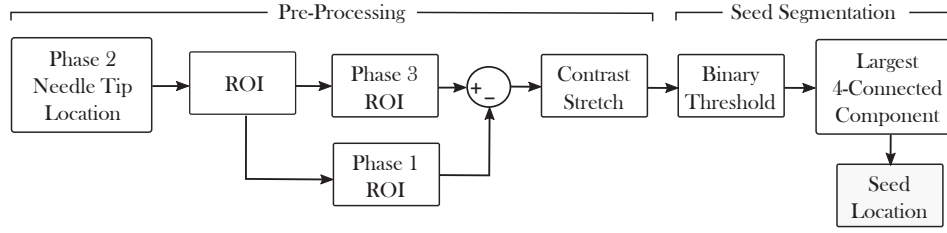
(a) Seed segmentation routine
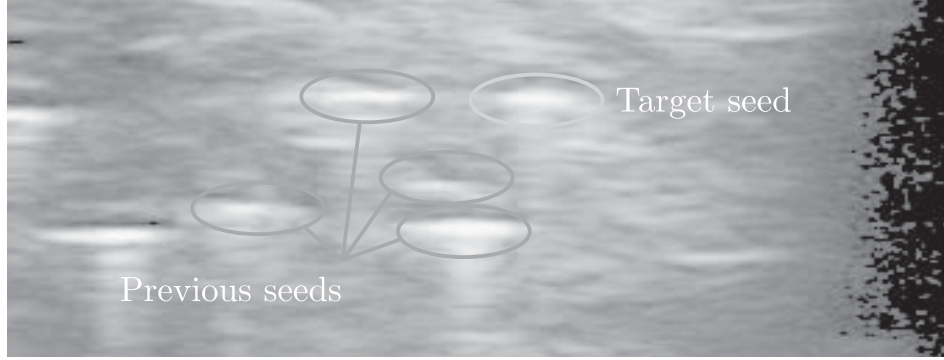
Phase 3 original image
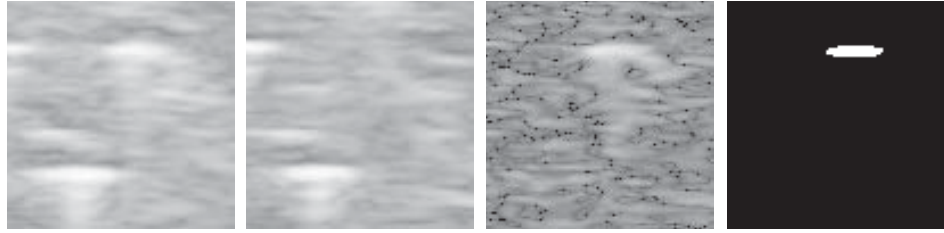
Phase 3 ROI   Phase 1 ROI   Enhanced   Binary

(b) Example of ultrasound image processing

Figure 7: Seed tracking routine in ultrasound images (a). The image processing is presented in (b). Ultrasound images captured during a Phase 3 showing the last implanted seed to be localized, with the tracking algorithm steps shown underneath.

instead be maintained stationary at the maximal insertion depth to measure the needle deflection at a single depth.

Following the procedure described in Section III, the force applied at the needle tip is identified. The obtained force is input to the needle-tissue interaction model Rossa et al. (2016) and the needle deflection is estimated for various candidate tissue stiffness values. The optimal needle-tissue stiffness is the one that minimizes the difference between the predicted and observed needle tip deflection at the maximal insertion depth. Figure 5 presents the results obtained with the identified model parameters. The prediction er-

Table 1: Indentified needle tip force (N), tissue stiffness (N·mm^{-2}), and average absolute prediction error (mm).

|	Porcine tissue	Bovine tissue	Synthetic tissue
Force	1.10 ±0.07	1.26 ±0.05	0.78 ±0.12
Stiffness	72.6	86.5	36.6
Mean error	0.53 ±0.28	0.83 ±0.44	0.89 ±0.62

ror is less than 1 mm for all tissue samples. The results, including the optimal tissue stiffness, are summarized in Table 1.

5.2 Seed Implant with Non-image Based Needle Steering

Knowing all the parameters necessary for estimating the needle tip trajectory, the depths of rotation are determined by the controller. Let us first assume that no image feedback is available. Therefore, the controller is only used prior to the needle insertion. The needle is inserted through the grid template at different locations spaced 5 mm apart as in current clinical brachytherapy. 15 insertions are performed followed by seed deposition. The path followed by the needle tip is shown in Fig. 6(a) along with the orientation of the needle bevel angle. Over 45 insertions, the average needle targeting accuracy in the X and Y directions is 0.93 and 0.62 mm with the highest error occurring in bovine tissue and the lowest error observed in porcine tissue.

Once the needle reaches the depth of 140 mm, the seed loaded in the needle shaft is deposited in tissue and the needle is withdrawn. The final seed location with respect to the desired hypothetical seed distribution is shown in Fig. 8(a). The gray solid dot indicates the desired seed location, which is defined as a point in a 2D plane parallel to the grid template at a depth of 140 mm. The final needle tip location is shown by the blue circle and the square is centroid of each seed after needle withdrawal. The average seed targeting accuracy in the X and Y planes is 0.89 and 0.60 mm, respectively. During needle withdrawal the tissue deforms and moves the seeds by up to 0.30 mm see (Fig. 9). These results are summarized in Table 2.
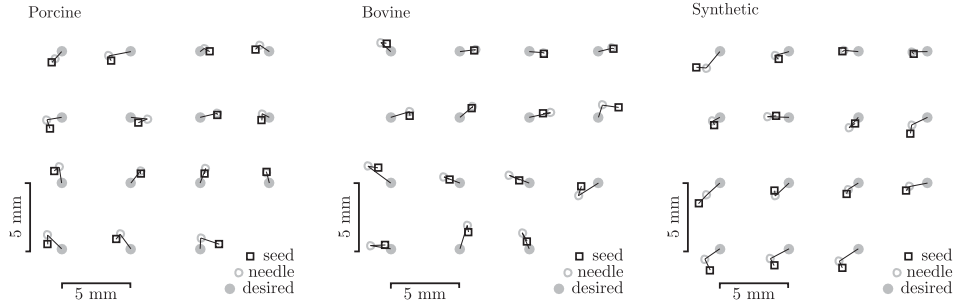
(a) Targeting accuracy and final seed location with open loop needle steering.
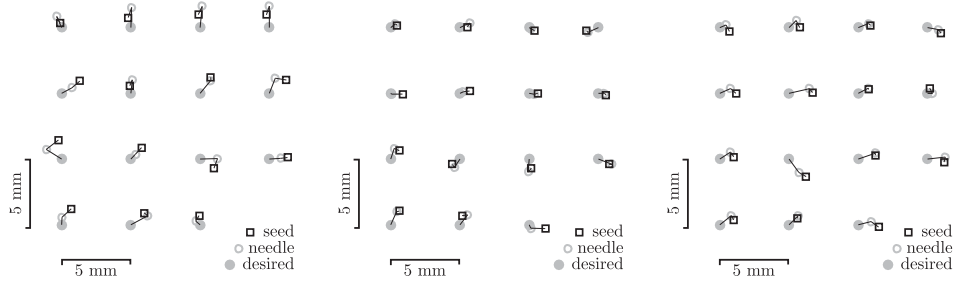
(b) Targeting accuracy and final seed location with closed loop needle steering.

Figure 8: Experimental results of seed deposition following a hypothetical pre-planning. The solid gray dot indicates the seed target location. The blue circle is the position of the needle tip at the target depth, and the dark square shows the final position of the centroid of each seed after the needle is withdrawn.

5.3 Seed Implant with Image-based Needle Steering

Let us now assume that the position of the needle tip can be measured at any time during insertion from ultrasound images. As a result, the steering controller can update the optimal rotation depths on-line. This is expected to result in an immediate improvement of targeting accuracy since the controller replans the path towards the target given the current position of the needle tip X_0, and the number n of axial rotations that have been performed.

The path followed by the needle tip is presented in Fig. 6(b). The third panel shows the *average* position of the bevel angle. The absolute needle targeting accuracy in the X and Y planes is 0.57 and 0.53 mm, respectively. Considering the deflection along X, this corresponds to an improvement of 40% compared to the case without image feedback. The final needle tip location at the target depth and the final location of the deposited seeds are shown in Fig. 8(b).

Table 2: Experiential results. Average absolute needle targeting accuracy, seed placement error and seed deviation after needle withdrawal, and average depth of needle rotation. Units are in millimetres.

		Porcine tissue	Bovine tissue	Synthetic tissue	Average
non-image based	X needle	0.69 ±0.45	1.07 ±0.41	1.05 ± 0.28	0.93
	Y needle	0.63 ±0.38	0.68 ±0.48	0.56 ± 0.38	0.62
	X seed	0.81 ±0.36	0.86 ±0.38	1.01 ± 0.46	0.89
	Y seed	0.53 ±0.30	0.46 ±0.37	0.81 ± 0.53	0.60
	X motion	0.27 ±0.34	0.40 ±0.37	0.29 ± 0.21	0.32
	Y motion	0.35 ±0.17	0.22 ±0.23	0.36 ± 0.23	0.31
	Rotation 1	31.1	18.7	12.8	
	Rotation 2	51.3	40.5	49.1	
	Rotation 3	100.9	102.5	118.9	
image based	X needle	0.51 ±0.44	0.39 ±0.26	0.81 ± 0.30	**0.57**
	Y needle	0.79 ±0.52	0.41 ±0.34	0.40 ± 0.25	0.53
	X seed	0.60 ±0.48	0.59 ±0.25	0.21 ± 0.89	**0.46**
	Y seed	0.84 ±0.34	0.34 ±0.29	0.31 ± 0.31	0.49
	X motion	0.38 ±0.24	0.31 ±0.26	0.21 ± 0.21	0.30
	Y motion	0.47 ±0.22	0.11 ±0.09	0.31 ± 0.31	0.29
	Rotation 1	39.2 ±12.4	36.8 ±9.3	38.2 ±7.7	
	Rotation 2	52.4 ±13.7	49.6 ±11.9	55.2 ±10.3	
	Rotation 3	98.5 ±16.4	122 ±15.8	95.8 ±12.2	

The average deviation from the actual to the desired seed location is 0.46 and 0.49 mm in the vertical and horizontal planes, respectively. The second part of Table 2 summarizes these results.

5.4 Discussion

Two different approaches have been proposed to steer a seed-carrying needle towards a pre-defined target. In the first approach the needle steering apparatus rotates the needle base at optimally depths determined preoperatively. In the second case, the the current position of the needle tip is used to update the optimal rotation depths intraoperatively.

The first method is compatible with a clinical setting where real-time measurement of the needle tip cannot be obtained during insertion. To address this limitation the steering apparatus is
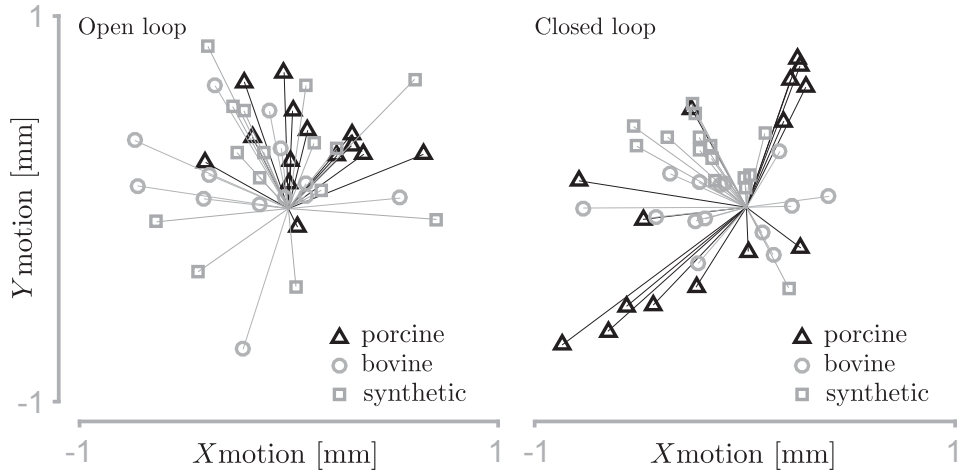
Figure 9: Dummy seed displacement from the deposition location during needle withdrawal in each tissue with open loop (left) and closed loop (right) needle steering controllers.

equipped with a force sensor that measures the needle insertion and withdrawal forces and estimates the required model parameters using the deflection measured at a single depth after insertion. 15 seeds are implanted 5 mm apart in the tissue to form a hypothetical seed distribution. The average needle and seed targeting accuracy in the controlled deflection direction is 0.93 and 0.89 mm on average, respectively.

The second method uses ultrasound images to measure the needle tip deflection in tissue as it is inserted. The controller running at 1 Hz recalculates the steering manoeuvres online, such that deviations from the offline predicted path can be corrected. With this approach, the average seed placement error is reduced to 0.46 mm.

Some commercially available ultrasound systems can be employed to follow the needle tip during insertion. Examples include the TargetScan from Envisioneering Medical, Overland, USA, where the 2D axial imaging plane translates within a stationary transrectal probe, and the 3D-2052 ultrasound probe from B&K Ultrasound. Peabody, USA, where the imaging plane translates axially by 70 mm. As an alternative, the Sonalis Ultrasound System from Best Medical, Pittsburgh, USA, has a longitudinal array that provides for 140 mm length of view, encompassing the bladder, the prostate and the perineum. Hence, the needle can be observed during throughout the insertion as long as it does not deflect out of the imaging plane.

Standards for seed implant quality are typically defined in terms of quantitative X-ray Computed Tomography-based postoperative

dosimetric evaluation. Currently, ultrasound-based postoperative seed identification cannot be done routinely with any better than 80% accuracy Han et al. (2003); Wei et al. (2006). CT-based dosimetry evaluation requires a separate imaging session to scan the patient prostate in order to determine the final location of the seeds. This assessment is subject to anatomical variations of the prostate position and postoperative edema of the prostate gland. With the proposed method in this paper, assessment and corrections regarding seed implantation errors can be taken during the procedure without the need for postoperative imaging.

6. Conclusion

In this paper we demonstrate the feasibility of a new framework for accurate radioactive seed implantation and tracking during low dose rate prostate brachytherapy for prostate cancer. A hand-held needle steering apparatus controls the deflection of a seed-carrying needle during insertion such that the needle tip reaches the desired target with minimum deflection. The steering controller evaluates the effects of axial needle rotations at different depths on the needle targeting accuracy via a needle-tissue interaction model. Optimal rotation depths are determined prior to the procedure and can be updated as the needle insertion progresses. The device *automatically* steers the needle as the surgeon *manually* inserts it in tissue, keeping the surgeon in control of the procedure. Once the needle reaches the target, the surgeon can deposit the seeds in tissue as in current clinical practice. Hence, the proposed framework does not require major modifications to the operating room setup. Knowing the final needle tip location prior to seed deposition, a method is proposed to track the final seed locations after needle withdrawal, allowing the surgeon to monitor implant quality on the fly.

Despite the current clinical individual seed placement uncertainty of 5 mm, very good clinical results for brachytherapy can be achieved when the whole prostate gland is treated. This is a consequence of the large number of seeds involved in a whole gland implant (typically 80 to 100), and the addition of a 3 mm margin around the prostate to create a planning target volume to which the treatment dose is prescribed Salembier et al. (2007). With the proposed system, the average seed placement accuracy is improved to 0.46 mm in tissue phantoms. Reducing seed placement error to this order in the clinic can enable accurate brachytherapy boost or focal treatment of dominant intra-prostatic lesions rather than

treating the whole prostate gland. Seeds carrying higher radiation doses can be considered to reduce the number of implanted seeds and the targeted areas within the prostate.

Combined with improved imaging techniques Atri et al. (2009), it is possible to identify men with low- to intermediate-risk prostate cancer who have low volume focal disease and who may be suitable for local therapy. This would result in fewer side effects to the patient including reduced urinary problems, rectal symptoms, and improved erectile function Langley et al. (2012). In addition, the possibility of post-treatment after focal brachytherapy is expected to be easier than after conventional treatment of the whole prostate gland. Among the options for such treatment, it is possible to treat remaining regions of the prostate volume with specific techniques of external irradiation or salvage surgery Cosset et al. (2013).

Competing Interests

None to declare.

Funding

References

Adebar, T., Salcudean, S., Mahdavi, S., Moradi, M., Nguan, C. et al. (2011). A robotic system for intra-operative transrectal ultrasound and ultrasound elastography in radical prostatectomy. In Information Processing in Computer-Assisted Interventions, pp. 79–89.

Atri, M., Gertner, M., Haider, M., Weersink, R., Trachtenberg, J. (2009). Contrast-enhanced ultrasonography for real-time monitoring of interstitial laser thermal therapy in the focal treatment of prostate cancer. Canadian Urological Association Journal, 3(2): 125–30.

Basu, S., Tsai, J. and Majewicz, A. (2016). Evaluation of tactile guidance cue mappings for emergency percutaneous needle insertion. In IEEE Haptics Symposium.

Bott, S., Ahmed, H., Hindley, R., Abdul-Rahman, A., Freeman, A. et al. (2010). The index lesion and focal therapy: An analysis of the pathological characteristics of prostate cancer. BJU International, 106(11): 1607–1611.

Cosset, J. -M., Cathelineau, X., Wakil, G., Pierrat, N., Quenzer, O. et al. (2013). Focal brachytherapy for selected low-risk prostate cancers: A pilot study. Brachytherapy, 12(4): 331–337.

Cowan, N., Goldberg, K., Chirikjian, G., Fichtinger, G., Alterovitz, R. et al. (2011). Robotic needle steering: Design, modeling, planning, and image guidance. In Surgical Robotics, pp. 557–582.

Fichtinger, G., Fiene, J., Kennedy, C., Kronreif, G., Iordachita, I. et al. (2008). Robotic assistance for ultrasound-guided prostate brachytherapy. Medical Image Analysis, 12(5): 535–545.

Han, B., Wallner, K., Merrick, G., Butler, W., Sutlief, S. et al. (2003). Prostate brachytherapy seed identification on post-implant trus images. Medical Physics, 30(5): 898–900.

Hungr, N., Baumann, M., Long, J. -A. and Troccaz, J. (2012). A 3D ultrasound robotic prostate brachytherapy system with prostate motion tracking. Robotics, IEEE Transactions on 28(6): 1382–1397.

Karavitakis, M., Winkler, M., Abel, P., Livni, N., Beckley, I. et al. (2011). Histological characteristics of the index lesion in whole-mount radical prostatectomy specimens: Implications for focal therapy. Prostate Cancer and Prostatic Diseases, 14(1): 46–52.

Khadem, M., Rossa, C., Sloboda, R. S., Usmani, N., Tavakoli, M. et al. (2016). Mechanics of tissue cutting during needle insertion in biological tissue. IEEE Robotics and Automation Letters, 1(2): 800–807.

Khadem, M., Rossa, C., Usmani, N., Sloboda, R. S., Tavakoli, M. et al. (2016). A two-body rigid/flexible model of needle steering dynamics in soft tissue. IEEE/ASME Transactions on Mechatronics, 99: 1–1.

Langley, S., Ahmed, H. U., Al-Qaisieh, B., Bostwick, D., Dickinson, L. et al. (2012). Report of a consensus meeting on focal low dose rate brachytherapy for prostate cancer. BJU International, 109(s1): 7–16.

LaValle, S. M. and Kuffner, J. J. (2001). Randomized kinodynamic planning. The International Journal of Robotics Research, 20(5): 378–400.

Magee, D., Zhu, Y., Ratnalingam, R., Gardner, P., Kessel, D. et al. (2007). An augmented reality simulator for ultrasound guided needle placement training. Medical & Biological Engineering & Computing, 45(10): 957–967.

Meltsner, M., Ferrier, N. J. and Thomadsen, B. (2007). Observations on rotating needle insertions using a brachytherapy robot. Physics in Medicine and Biology, 52(19): 6027.

Muntener, M., Patriciu, A., Petrisor, D., Mazilu, D., Bagga, H. et al. (2006). Magnetic resonance imaging compatible robotic system for fully automated brachytherapy seed placement. Urology, 68(6): 1313–1317.

Nath, S., Chen, Z., Yue, N., Trumpore, S., Peschel, R. et al. (2000). Dosimetric effects of needle divergence in prostate seed implant using 125i and 103pd radioactive seeds. Medical Physics, 27(5): 1058–1066.

Patil, S. et al. (2014). Needle steering in 3D via rapid replanning. IEEE Transactions on Robotics, 30(4): 853–864.

Patriciu, A., Petrisor, D., Muntener, M., Mazilu, D., Schar, M. et al. (2007). Automatic brachytherapy seed placement under mri guidance. IEEE Transactions on Biomedical Engineering, 54(8): 1499–1506.

Phee, L., Yuen, J., Xiao, D., Chan, C. F., Ho, H. et al. (2006). Ultrasound guided robotic biopsy of the prostate. International Journal of Humanoid Robotics, 3(04): 463–483.

Podder, T., Beaulieu, L., Caldwell, B., Cormack, R., Crass, J. et al. (2014). AAPM and GEC-ESTRO guidelines for image-guided robotic brachytherapy: Report of task group 192. Medical Physics, 41(10): 101501.

Rossa, C., Fong, J., Usmani, N., Sloboda, R., Tavakoli, M. et al. (2016). Multi-actuator haptic feedback on the wrist for needle steering guidance in brachytherapy. IEEE Robotics and Automation Letters, 99: 1–1.

Rossa, C., Khadem, M., Sloboda, R., Usmani, N., Tavakoli, M. et al. (2016). Adaptive quasi-static modelling of needle deflection

during steering in soft tissue. IEEE Robotics and Automation Letters, 1(2): 916–923.

Rossa, C., Usmani, N., Sloboda, R. and Tavakoli, M. (2016). A hand-held assistant for semi-automated percutaneous needle steering. IEEE Transactions on Biomedical Engineering In Press.

Salcudean, S., Prananta, T., Morris, W. and Spadinger, I. (2008). A robotic needle guide for prostate brachytherapy. In Robotics and Automation, 2008. ICRA 2008. IEEE International Conference on, pp. 2975–2981.

Salembier, C., Lavagnini, P., Nickers, P., Mangili, P., Rijnders, A. et al. (2007). Tumour and target volumes in permanent prostate brachytherapy: A supplement to the estro/eau/eortc recommendations on prostate brachytherapy. Radiotherapy and Oncology, 83(1): 3–10.

Schneider, C., Okamura, A. and Fichtinger, G. (2004). A robotic system for transrectal needle insertion into the prostate with integrated ultrasound. In IEEE International Conference on Robotics and Automation, 1: 365–370.

Seifabadi, R., Song, S., Krieger, A., Cho, N., Tokuda, J. et al. (2012). Robotic system for mri-guided prostate biopsy: Feasibility of teleoperated needle insertion and ex vivo phantom study. International Journal of Computer Assisted Radiology and Surgery, 7(2): 181–190.

Sloboda, R., Usmani, N., Pedersen, J., Murtha, A., Pervez, N. et al. (2010). Time course of prostatic edema post permanent seed implant determined by magnetic resonance imaging. Brachytherapy, 9(4): 354–361.

Taschereau, R., Pouliot, J., Roy, J. and Tremblay, D. (2000). Seed misplacement and stabilizing needles in transperineal permanent prostate implants. Radiotherapy and Oncology, 55(1): 59–63.

Usmani, N., Chng, N., Spadinger, I. and Morris, W. J. (2011). Lack of significant intraprostatic migration of stranded iodine-125 sources in prostate brachytherapy implants. Brachytherapy, 10(4): 275–285.

Waine, M., Rossa, C., Sloboda, R., Usmani, N. and Tavakoli, M. (2016). Needle tracking and deflection prediction for robot-

assisted needle insertion using 2d ultrasound images. Journal of Medical Robotics Research, 01(01): 1640001.

Webster, R. J., Kim, J. S., Cowan, N. J., Chirikjian, G. S., Okamura, A. M. et al. (2006). Nonholonomic modeling of needle steering. The International Journal of Robotics Research, 25(5-6): 509–525.

Wei, Z., Wan, G., Gardi, L., Mills, G. and Downey, D. (2004). Robot-assisted 3D-TRUS guided prostate brachytherapy: System integration and validation. Medical Physics, 31(3): 539–548.

Wei, Z., Gardi, L., Downey, D. and Fenster, A. (2006). Automated localization of implanted seeds in 3d trus images used for prostate brachytherapy. Medical Physics, 33(7): 2404–2417.

Yu, Y., Podder, T., Zhang, Y., Ng, W. -S., Misic, V. et al. (2006). Robot-assisted prostate brachytherapy. In Medical Image Computing and Computer-Assisted Intervention, pp. 41–49.